Q-band Polarizers for the LSPE-Strip Correlation Radiometric Instrument

O. A. Peverini[a], M. Lumia[a], Z. Farooqui[a], G. Addamo[a], G. Virone[a], F. Paonessa[a] , L. Ciorba[a], M. Zannoni[b,c], M. Gervasi[b,c], C. Franceschet[d,e], M. Bersanelli[d,e], A. Mennella[d,e], F. Cuttaia[f], G. Morgante[f], F. Villa[f] and M. Jones[g]

[a] *CNR-IEIIT, c/o Politecnico di Torino, Corso Duca degli Abruzzi 24, 10129 Torino, Italy*
[b] *Università degli Studi di Milano-Bicocca, Piazza della Scienza 3, 20126 Milano, Italy*
[c] *INFN–Sezione di Milano Bicocca, Piazza della Scienza 3, 20126 Milano, Italy*
[d] *Università degli Studi di Milano, Via Celoria 16, 20133 Milano, Italy*
[e] *INFN Sezione di Milano, Via Celoria 16, 20133 Milano, Italy*
[f] *INAF-OAS Bologna, Via Gobetti 101, 40129 Bologna, Italy*
[g] *University of Oxford, Denys Wilkinson Building, Keble Road, Oxford OX1 3RH, UK*

E-mail: oscar.peverini@ieiit.cnr.it

ABSTRACT: This paper reports the design, manufacturing and testing of the cluster of polarizers developed for the LSPE-Strip correlation receiver array working in the Q band (39-48 GHz). Since the LSPE experiment targets the measurement of the very faint B-mode component of the Cosmic Microwave Background, the electromagnetic design of the polarizers was conceived in view of minimizing the measurement uncertainties introduced by the polarizers in the LSPE-Strip dual-circular-polarization correlation receiving chain. To this end, the main figures-of-merit of the LSPE-Strip polarizers were derived in terms of the Mueller sub-matrices relating the relevant input and output Stokes parameters. As a result, a dual-ridge layout, in which stepped-ridge discontinuities are interleaved with grooved cavities, was selected. The heights of both the stepped discontinuities and the grooved cavities were considered as design degrees of freedom in order to minimize the differential phase-error between the two principal polarizations of the polarizer w.r.t the ideal 90-deg value. The latter condition is the one required for converting the incoming circular polarizations into two linearly polarized ones. The polarizer design allows for a complete manufacturing route (mechanical layout, machining process and assembling) exhibiting high accuracy (< 10 μm) for all the units. As a consequence, the measured performance of the whole polarizer cluster is in tight agreement with predictions. Notably, the in-band mean value of the spurious conversion from the total intensity *I* to the two linearly polarized Stokes parameters *Q* and *U* introduced by the polarizers is smaller than -28 dB (mean value of fifty-one polarizers) with a standard deviation less than 1 dB.

KEYWORDS: Instruments for CMB observations, Passive components for microwaves, Microwave radiometers, Polarizers, Polarimeters.

Contents

1. Introduction

The Cosmic Microwave Background (CMB) represents a unique observational window into the early universe. Over the years, increasingly accurate observations have provided a cornerstone of the standard cosmological model and have led to accurate determination of the fundamental cosmological parameters (see [1], and references therein). Currently several new-generation experiments are being developed specifically devoted to the search for the B-mode component in the CMB polarization pattern as a probe of the inflation era (see [2] for a review). The extremely low level of the B-mode signal (a fraction of a micro-Kelvin) requires the extreme rejection of systematic effects and multi-frequency observations to accurately remove polarized foregrounds (mainly synchrotron at frequencies below 100 GHz and polarized dust at higher frequencies). The Large Scale Polarization Explorer (LSPE) program [3] covers five frequencies in the range 40-240 GHz with a combination of two instruments: the Strip ground-based telescope, based on dual-circular correlation receivers, covers the 44 GHz band, with an atmospheric monitor at 90 GHz; the SWIPE balloon-borne instrument operates in the 145 GHz, 220 GHz, and 240 GHz bands with bolometric receivers. The Strip radiometer design, in particular, ensures rejection of systematic effects taking advantage of the high polarization purity achievable with coherent devices and waveguide components.

In this paper we describe in detail the design, manufacturing and experimental characterization of the cluster of forty-nine waveguide polarizers operating in the LSPE-Strip 39-48 GHz band. The paper outline is as follows. Section 2 reports an overview of the LSPE-Strip polarimeter design, highlighting the key role of the polarizers. In section 3, the electromagnetic and mechanical designs are discussed with reference to the main figures-of-merit of the polarizers for the LSPE-Strip instrument. Additionally, an ad-hoc assembly procedure for the fine tuning of the polarizers' performance is reported. Finally, section 4 and section 5 respectively report the measured performance of the polarizer prototype and of the entire cluster of forty-nine elements.

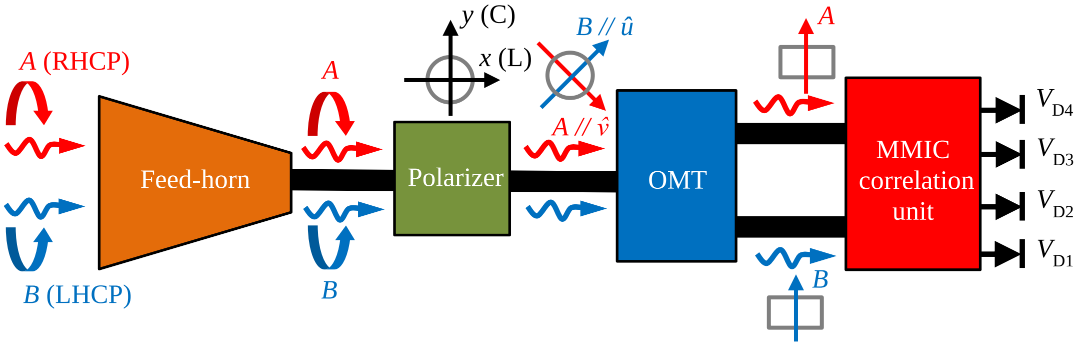

Figure 1. Block diagram of the LSPE-STRIP Q-band circular-polarization correlation receiver.

2. The LSPE-Strip Instrument

The LSPE-Strip instrument is designed to simultaneously detect the *Q* and *U* Stokes parameters of the incoming radiation through two arrays of dual-circular correlation receivers operating in Q and W bands. The LSPE-Strip instrument will be installed in the focal plane of a dual-reflector crossed-Dragone telescope (with a projected aperture of approximately 1.5 m) at the Teide Observatory in Tenerife [3]. The Q-band array consists of forty-nine correlation receivers operating from 39 GHz to 48 GHz (20% bandwidth) and cooled to 20 K.

The LSPE-Strip instrument is an array of correlation radiometers in which the incident electromagnetic field, $\underline{E}$, is processed in the circular-polarization basis, *i.e.*, $\underline{E} = A\,\underline{\hat{e}}_{\mathrm{RHCP}} + B\,\underline{\hat{e}}_{\mathrm{LHCP}}$, where $\underline{\hat{e}}_{\mathrm{RHCP}} = (\hat{x}\text{-}j\hat{y})/\sqrt{2}$ and $\underline{\hat{e}}_{\mathrm{LHCP}} = (\hat{x}+j\hat{y})/\sqrt{2}$ are the Right(Left)-Hand Circular Polarizations (RHCP, LHCP) unit vectors. For a linearly-polarized field $\underline{E}^{(\mathrm{LP})}$aligned along the direction θ w.r.t. the x axis, $A = E^{(\mathrm{LP})}e^{j\theta}/\sqrt{2}$ and $B = E^{(\mathrm{LP})}e^{-j\theta}/\sqrt{2}$. As shown in the block diagram of the correlation receivers in Figure 1, both circular-polarization components *A* and *B* of the radiation collected by the reflector enter each of the forty-nine corrugated feed-horns [4]. The latter are arranged into a lattice of seven hexagonal modules, each including seven elements placed in the focal plane.

In each receiver chain, the two circularly-polarized components *A* and *B* of the incoming radiation at the output port of the feed horn are converted by means of a polarizer into two linear polarizations aligned along the $\hat{v}$ and $\hat{u}$ axes of the common circular waveguide. Since the latter directions are rotated by 45° w.r.t the inductive (L // $\hat{x}$) and capacitive (C // $\hat{y}$) principal directions of the polarizer [5], the platelet Ortho-Mode Transducer (OMT) described in [6] is rotated by 45° w.r.t the principal axes L and C of the polarizer. The two signals extracted by the OMT are routed to the input ports of the Monolithic Microwave Integrated Circuit (MMIC) that implements the correlation, and then to two High Electron Mobility Transistor (HEMT) amplifiers. All the MMIC correlation units are based on the layout designed for the QUIET experiment [7], 16 Q-band units having already been tested and used in the QUIET instrument.

In the operative basis of the instrument, the transmission block $\boldsymbol{S}_{21}$ of the polarizer scattering matrix defines the relationship

$$\begin{bmatrix} b_{2,\mathrm{v}} \\ b_{2,\mathrm{u}} \end{bmatrix} = \boldsymbol{S}_{21} \cdot \begin{bmatrix} a_{1,\mathrm{RHCP}} \\ a_{1,\mathrm{LHCP}} \end{bmatrix}, \qquad (1.1)$$

where ports 1 and 2 are the polarizer ports towards the feed-horn and the OMT, respectively. For a lossless and perfectly matched polarizer, the $\boldsymbol{S}_{21}$ sub-matrix is an identity matrix, such that each circularly-polarized component (A or B) is entirely coupled to the corresponding nominal linear polarization (along the $\hat{v}$ or $\hat{u}$ axes). This condition can be guaranteed by introducing a differential phase-shift $\bar{\phi}$ of 90 deg between the two linear polarizations aligned with the principal inductive and capacitive axes of the polarizer [5]. Accordingly, for an ideal polarizer the transmission sub-matrix $\hat{\boldsymbol{S}}_{21}$ in the principal-axes basis is given by

$$\begin{bmatrix} b_{2,\mathrm{L}} \\ b_{2,\mathrm{C}} \end{bmatrix} = \hat{\boldsymbol{S}}_{21} \cdot \begin{bmatrix} a_{1,\mathrm{L}} \\ a_{1,\mathrm{C}} \end{bmatrix} = e^{+j\varphi} \begin{bmatrix} e^{+\frac{j\pi}{2}} & 0 \\ 0 & 1 \end{bmatrix} \cdot \begin{bmatrix} a_{1,\mathrm{L}} \\ a_{1,\mathrm{C}} \end{bmatrix}. \tag{1.2}$$

The MMIC correlation unit provides four output signals that are proportional to the in-phase and quadrature sums and differences of the circular components A and B:

$$\begin{aligned} V_{\mathrm{D1}} &\propto \langle |A+B|^2 \rangle \\ V_{\mathrm{D2}} &\propto \langle |A-B|^2 \rangle \\ V_{\mathrm{D3}} &\propto \langle |A+jB|^2 \rangle \\ V_{\mathrm{D4}} &\propto \langle |A-jB|^2 \rangle. \end{aligned} \tag{1.3}$$

Recalling that the Stokes parameters can be expressed in terms of the circular components of the field via

$$\begin{aligned} Q &= \langle |E_x|^2 - |E_y|^2 \rangle = \langle 2\Re\{AB^*\} \rangle \\ U &= \langle 2\Re\{E_x E_y^*\} \rangle = \langle 2\Im\{AB^*\} \rangle \\ V &= \langle \text{-}2\Im\{E_x E_y^*\} \rangle = \langle |B|^2 - |A|^2 \rangle \\ I &= \langle |E_x|^2 + |E_y|^2 \rangle = \langle |A|^2 + |B|^2 \rangle, \end{aligned} \tag{1.4}$$

where $\langle \cdots \rangle$ represents the spectral average in the working band, $\Re\{\cdots\}$ and $\Im\{\cdots\}$ are the real and imaginary part operators, and $\{\cdots\}^*$ denotes the complex conjugate operator.

The Q and U Stokes parameters of the incoming signals can be measured by combining the four outputs of the MMIC correlation unit as

$$\begin{aligned} Q_{\mathrm{m}} &\propto V_{\mathrm{D1}} - V_{\mathrm{D2}} \\ U_{\mathrm{m}} &\propto V_{\mathrm{D3}} - V_{\mathrm{D4}}. \end{aligned} \tag{1.5}$$

In order to identify the key requirements for the LSPE-Strip receiver building blocks, the electromagnetic behavior of the entire receiver chain and of the stand-alone components were described in terms of the Mueller matrix $\boldsymbol{M}$ relating the input and output Stoke parameters

$$\begin{bmatrix} Q \\ U \\ V \\ I \end{bmatrix}_{\mathrm{out}} = \boldsymbol{M} \cdot \begin{bmatrix} Q \\ U \\ V \\ I \end{bmatrix}_{\mathrm{in}} = \begin{bmatrix} \boldsymbol{H} & \boldsymbol{K} \\ \boldsymbol{P} & \boldsymbol{N} \end{bmatrix} \cdot \begin{bmatrix} Q \\ U \\ V \\ I \end{bmatrix}_{\mathrm{in}} \tag{1.6}$$

Since the LSPE-Strip instrument aims at measuring the linear polarization state of the incoming signals, the sub-matrices of interest are $\boldsymbol{H}$ (connecting the input and output linearly-polarized components Q and U) and $\boldsymbol{K}$ (containing the spurious contamination caused by the circularly-polarized component V and by the total intensity I). These sub-matrices are defined by the relationship

$$\begin{bmatrix} Q \\ U \end{bmatrix}_{\text{out}} = \begin{bmatrix} H_{QQ} & H_{QU} \\ H_{UQ} & H_{UU} \end{bmatrix} \cdot \begin{bmatrix} Q \\ U \end{bmatrix}_{\text{in}} + \begin{bmatrix} K_{\text{QV}} & K_{QI} \\ K_{UV} & K_{UI} \end{bmatrix} \cdot \begin{bmatrix} V \\ I \end{bmatrix}_{\text{in}}. \quad (1.7)$$

The total intensity contains both the polarized and un-polarized components of the input signal, as well as the instrument noise referred at the antenna input. Since the latter component is several orders of magnitude higher than the linearly-polarized target signal, the receiver sensitivity to Q and U is largely dominated by the coefficients K_{QI} and K_{UI}. Hence, minimization of these spurious coefficients was a key requirement in the design of each building block of the LSPE-Strip receiver chain. Based on previous field experience on similar radiometer designs, a design goal for K_{QI} and K_{UI} of -25 dB was set. A dedicated analysis of residual leakage effects and mitigation strategies will be the subject of a forthcoming paper [8].

3. Polarizer Architecture

3.1 Main Figures-of-Merit for the LSPE-Strip Instrument

In order to identify the requirements to be addressed in the design of the polarizers, the blocks $\boldsymbol{H}$ and $\boldsymbol{K}$ of the Mueller-matrix (1.6) were derived in terms of the 2 × 2 transmission block $\hat{\boldsymbol{S}}_{\mathbf{21}}$ of the polarizer scattering matrix in the principal L- and C-axes basis

$$\hat{\boldsymbol{S}}_{\mathbf{21}} = \begin{bmatrix} T_{\text{LL}} & T_{\text{LC}} \\ T_{\text{CL}} & T_{\text{CC}} \end{bmatrix}. \quad (2.1)$$

As derived in [9], the coefficients of the direct-term sub-matrix $\boldsymbol{H}$ are

$$H_{QQ} = \tfrac{1}{2}\{|T_{\text{LL}}|^2 + |T_{\text{CC}}|^2 - |T_{\text{LC}}|^2 - |T_{\text{CL}}|^2\} \quad (2.2)$$

$$H_{QU} = \Re\{T_{\text{LL}}T_{\text{LC}}^* - T_{\text{CL}}T_{\text{CC}}^*\} \quad (2.3)$$

$$H_{UQ} = \Im\{T_{\text{LL}}T_{\text{CL}}^* - T_{\text{LC}}T_{\text{CC}}^*\} \quad (2.4)$$

$$H_{UU} = \Im\{T_{\text{LL}}T_{\text{CC}}^* + T_{\text{LC}}T_{\text{CL}}^*\}, \quad (2.5)$$

whereas the entries of the spurious contamination sub-matrix $\boldsymbol{K}$ are

$$K_{QI} = \tfrac{1}{2}\{|T_{\text{LL}}|^2 - |T_{\text{CL}}|^2 + |T_{\text{LC}}|^2 - |T_{\text{CC}}|^2\} \quad (2.6)$$

$$K_{QV} = \Im\{T_{\text{LL}}T_{\text{LC}}^* - T_{\text{CL}}T_{\text{CC}}^*\} \quad (2.7)$$

$$K_{UI} = \Im\{T_{\text{LL}}T_{\text{CL}}^* + T_{\text{LC}}T_{\text{CC}}^*\} \quad (2.8)$$

$$K_{UV} = -\Re\{T_{\text{LL}}T_{\text{CC}}^* - T_{\text{LC}}T_{\text{CL}}^*\}. \quad (2.9)$$

Eq.s (2.2)-(2.9) provide useful guidelines for the electromagnetic/mechanical design and the manufacturing of the polarizers. Indeed, equations (2.3) and (2.4) imply that the cross-polarization (X-pol.) transmission coefficients T_{LC} and T_{CL} should be as low as possible in order to correctly detect the polarization angle in the Q-U plane (*i.e.*, $H_{QU} = H_{UQ} \approx 0$). This condition is satisfied if the polarizer geometry exhibits a two-fold symmetry w.r.t the principal polarization axes (*i.e.*, xz and yz are symmetry planes of the component). Hence, if a highly accurate manufacturing route (i.e., mechanical layout, machining process and assembling) preserving the two-fold symmetry of the polarizer structure is selected, (2.2)-(2.9) simplify as

$$H_{QQ} = \tfrac{1}{2}\{|T_{\text{LL}}|^2 + |T_{\text{CC}}|^2\} \quad (2.10)$$

$$H_{QU} = H_{UQ} \approx 0 \quad (2.11)$$

$$H_{UU} = \Im\{T_{\text{LL}}T_{\text{CC}}^*\} \quad (2.12)$$

$$K_{QI} = \tfrac{1}{2}\{|T_{\text{LL}}|^2 - |T_{\text{CC}}|^2\} \quad (2.13)$$

$$K_{QV} = K_{UI} \approx 0 \quad (2.14)$$

$$K_{UV} = -\Re\{T_{\mathrm{LL}} T_{\mathrm{CC}}^{*}\}. \tag{2.15}$$

As can be seen in Equation (2.14), a high degree of two-fold symmetry in the polarizer leads also to the minimization of the spurious contamination coefficients K_{QV} and K_{UI}. With reference to coefficient K_{UI}, it can be proved that the condition $T_{\mathrm{LL}} T_{\mathrm{CL}}^{*} + T_{\mathrm{LC}} T_{\mathrm{CC}}^{*} = 0$ holds not only for a polarizer with zero X-pol. coefficients T_{LC} and T_{CL}, but in general for a perfectly-matched and lossless polarizer. Indeed, in the latter case, the transmission block $\hat{\boldsymbol{S}}_{\mathbf{21}}$ of the polarizer scattering matrix satisfies the condition $\hat{\boldsymbol{S}}_{\mathbf{21}} \cdot \hat{\boldsymbol{S}}_{\mathbf{21}}^{H} = \mathbf{0}$, where $\{\cdots\}^{H}$denotes the Hermitian conjugate operator. Hence, low values of reflection coefficients are beneficial for reducing the spurious contamination of the U parameter due to the total intensity I.

Eq.s (2.12) and (2.15) highlight that any deviation of the differential phase-shift ϕ between the inductive and capacitive co-polar transmission coefficients from the ideal value of 90 deg induces a leakage between the Stokes parameters U and V.

Finally, (2.13) shows that a precise matching of the insertion losses of the L and C polarizations is necessary to reduce the contamination of the total intensity over the Q parameter (coefficient K_{QI}).

3.2 Electromagnetic Design

Several polarizer geometries have been published in the technical literature, which differ in the type of discontinuities used for implementing the differential phase-shift between the principal polarizations and in the geometry of the common waveguide. The most common discontinuities are irises [10]-[13], grooves [14]-[16], and steps [17], which are inserted in circular, square or ridged waveguides. In order to achieve wide-band (above 20%) or dual-band operation, optimized shapes of the discontinuities [18], dielectric inserts [19]-[20], multi-ridge structures [21], and common waveguide cavities introducing additional phase-shifting [22] have been investigated. Recently, multi-stage polarizers consisting of a cascade of rotated quarter/half-wavelength sections have been developed [23]-[24] for achieving ultra-wide band operation (above 30%).

According to the main figures-of-merit derived in section 2.1, the selection of the polarizer layout for the LSPE-Strip Q-band array was carried out as a trade-off between both electromagnetic and mechanical aspects in view of manufacturing a large number of high-performance polarizers. The geometry of the final design is shown in Figure 2. It consists of a dual-ridge structure in circular waveguide with ridge thickness w = 1.5 mm. This value was selected as a compromise between mechanical robustness and performance in terms of reflection coefficients for the two principal polarizations. Eleven stepped discontinuities with heights $\{h_k^{(\mathrm{s})}\}$ and lengths $\{L_k^{(\mathrm{s})}\}$ were implemented in the ridges. Each cavity between two stepped-ridge discontinuities consists of a circular waveguide section with a groove in the two ridges. The lengths and heights of the grooves are $\{h_k^{(\mathrm{g})}\}$ and $\{L_k^{(\mathrm{g})}\}$, respectively. The profiles of the upper and lower ridges are identical in order to guarantee the two-fold symmetry w.r.t to the principal axes x (L) and y (C). To facilitate the machining of the ridge sections, the inner edges of the grooves were rounded with a radius r = 0.3 mm. The circular waveguide diameter was set to d = 6.8 mm so as to meet the single-mode condition from 25.9 GHz (cut-off frequency of the TE_{11} mode) up to 53.9 GHz (cut-off frequency of the TM_{11} mode). The TM_{10} and TE_{21} modes are nominally not excited because of the two-fold symmetry of the entire feed-chain. The low cut-off frequency of the TE_{11} mode was essential to achieve relatively low reflection coefficients (< -20 dB) down to 30 GHz. This out-of-band requirement at the component level

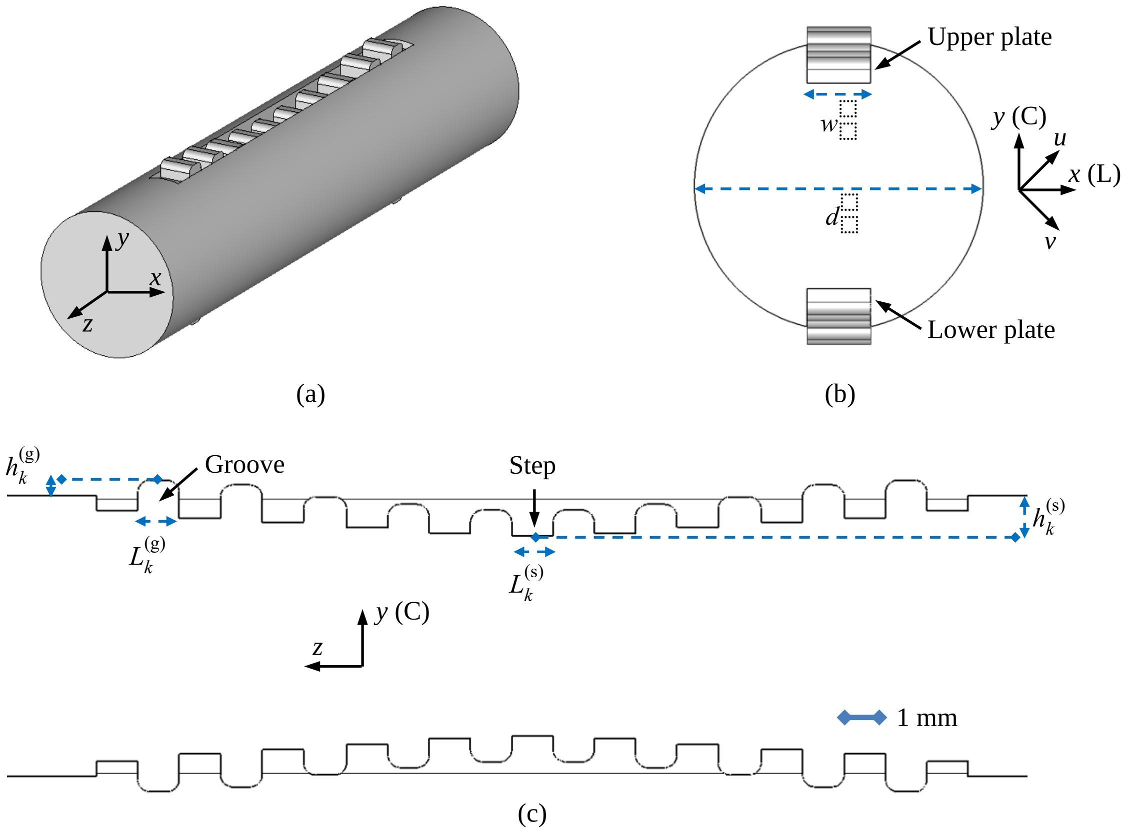

Figure 2. Inner waveguide structure of the polarizer. (a) 3D view. (b) Cut-view in the *x*-*y* plane. (c) Cut-view in the *y*-*z* plane.

was set in order to de-risk the generation of instabilities in the amplifiers caused by resonances within the receiver chain.

To minimize the deviation of the polarizer differential phase-shift $\bar{\phi}$ from the goal value of 90 deg, an approach similar to those presented in [18] and [22] was adopted. Specifically, the heights of both the steps $\{h_k^{(s)}\}_{k=1}^{11}$ and the grooves $\{h_k^{(g)}\}_{k=1}^{10}$ were considered as degrees of freedom to ensure optimal control of the relative phase-error ε_ϕ of each discontinuity. Figure 3(a) shows the contour map of the mean differential phase-shift $\bar{\phi}_k$ of each stepped discontinuity as a function of $h_k^{(s)}$ and $h_k^{(g)}$. The corresponding relative phase-error $\varepsilon_\phi = \frac{\Delta\phi_k}{\bar{\phi}_k}$ (%) (where $\Delta\phi_k$ is the in-band phase dispersion) is plotted in Figure 3(b). These electromagnetic parameters were computed by considering each stepped discontinuity as the unit cell of a periodic structure and selecting the corresponding propagating Bloch-wave [25]. In this way, the multi-modal interaction between the polarizer discontinuities is better accounted for than by considering each stepped discontinuity as a stand-alone structure. Figure 3(c) and Figure 3(d) show the contour maps of the reflection coefficients for the inductive (L-pol.) and capacitive (C-pol.) polarizations. In these analyses, the lengths of the stepped discontinuities $\{L_k^{(s)}\}$ and of the grooves $\{L_k^{(g)}\}$ were set to 1 mm. This value was verified to be the best compromise between electromagnetic performance and mechanical robustness.

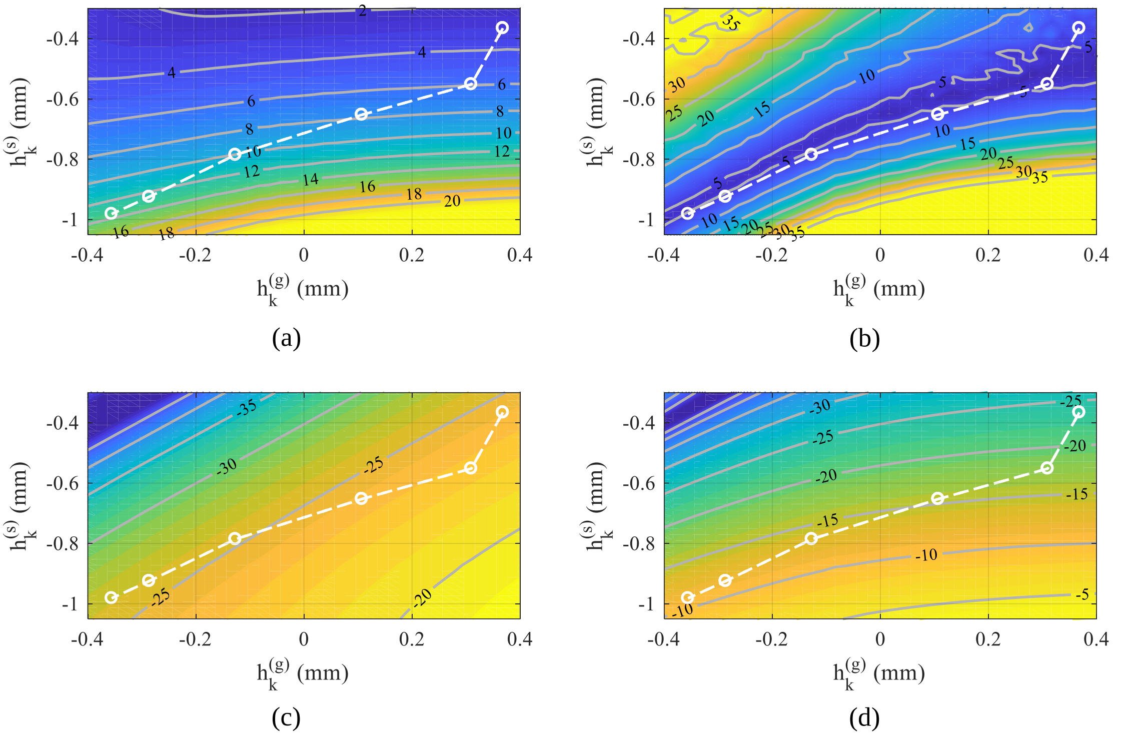

Figure 3. Contour maps of the main electrical parameters as a function of the step and groove heights for the polarizer geometry with ridge thickness w = 1.5 mm (see Figure 2). The white circles indicate the values of the first six stepped discontinuities of the designed polarizer geometry reported in the text. Only six circles are reported because of the polarizer symmetry w.r.t. to the longitudinal mid-point. (a) Mean in-band differential phase-shift $\overline{\phi}_k$ (deg). (b) Relative phase-error ε_ϕ (%). (c) Mean in-band reflection coefficient (dB) for the inductive polarization. (d) Mean in-band reflection coefficient (dB) for the capacitive polarization.

As can be inferred from the contour maps of Figure 3, varying the height of both the steps and the grooves guarantees that the required values of $\overline{\phi}_k$ will lie between 0 and 14 deg, while keeping the relative phase-error ε_ϕ below 5% for all the discontinuities. Based on these contour plots, the polarizer geometry was initially designed by combining the spectral-element simulation method described in [26] with the synthesis technique presented in [27]. The resulting geometry was, then, subjected to a fine optimization according to the minimax criterion $\min_{h_k}\left\{\max_{f}\{\alpha|S_{LL}|;\, \beta|S_{CC}|;\, \gamma\varepsilon_\phi\}\right\}$, where S_{LL} and S_{CC} are the reflection coefficients of the inductive and capacitive polarizations, and α, β, and γ are appropriate weighting coefficients. Specifically, $\alpha = 40$ dB, $\beta = 40$ dB, and $\gamma = 37$ dB were set in the final optimization. In the fine optimization stage, the polarizer geometry was constrained to be symmetrical w.r.t to the z axis. The corresponding values of $\{h_k^{(s)}\}$ and $\{h_k^{(g)}\}$ are

$$\left\{h_k^{(s)}\right\}_{k=1}^{6} = \{\text{-}0.366 \quad \text{-}0.552 \quad \text{-}0.653 \quad \text{-}0.786 \quad \text{-}0.925 \quad \text{-}0.982\} \text{ mm, and}$$

$$\left\{h_k^{(g)}\right\}_{k=1}^{5} = \{0.368 \quad 0.251 \quad \text{-}0.037 \quad \text{-}0.217 \quad \text{-}0.356\} \text{ mm.}$$

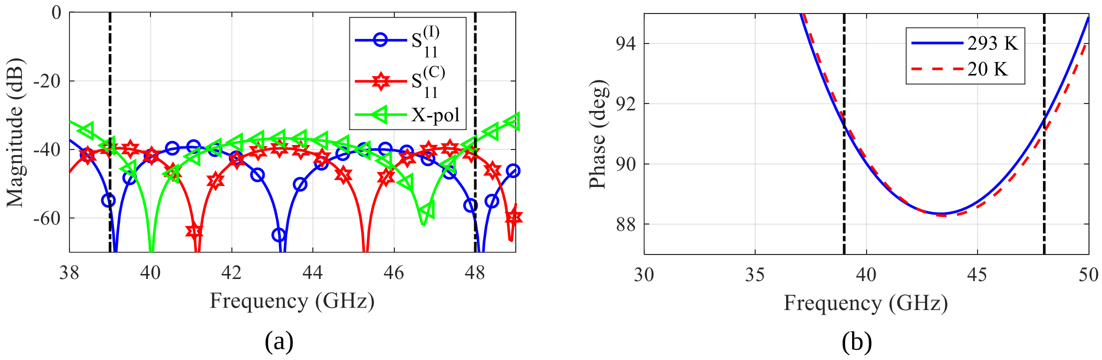

Figure 4. Predicted electromagnetic performance of the polarizer. (a) Reflection coefficients for the two principal polarizations and X-pol. transmission in the operative basis at 293 K. (b) Differential phase-shift $\bar{\phi}$ between the transmission coefficients in the principal-polarization basis at 20 K and 293 K.

The geometries of the periodic cell models corresponding to the optimized geometry are indicated in the four plots of Figure 3 by the six white circles.

The reflection coefficients of the final polarizer geometry for the two principal polarizations are lower than -39 dB (blue and red curves in Figure 4(a)), while the differential phase-shift $\bar{\phi}$ is 90 ± 1.7 deg (Figure 4(b)). This value corresponds to X-pol. transmission coefficients in the polarizer operative basis lower than -37 dB (green curve in Figure 4(a)). The electromagnetic performance of the polarizer was also computed at the operating temperature of 20 K in order to assess any degradation caused by thermal contraction. The polarizers are to be manufactured in 6061 aluminum alloy, which has a linear thermal expansion coefficient of -415.4 x 10^{-5} [28]. Almost no effects on the polarizer performance were shown when considering this thermal contraction, apart from the differential phase-shift being shifted up by 200 MHz (red dashed curve in Figure 4(b)). This aspect was properly accounted for by enlarging the design passband.

3.3 Mechanical Design

The mechanical design of the polarizer based on the inner waveguide structure of Figure 2 is shown in Figure 5(a). It consists of a split-block layout made of six parts: i) two input circular-waveguide lines (Line 1 and Line 2); ii) two covers (Covers 1 and Cover 2) for building up the main circular-waveguide section; and iii) two plates for implementing the upper and lower ridge-sections with the stepped/grooved profiles. This mechanical layout was selected because several units can be manufactured through milling and electrical-discharge machining at moderate lead time and cost with an accuracy better than 10 µm. Additionally, any performance degradation caused by small assembly errors can be easily recovered. An upward/downward shift of the ridge structures of the order of 10-20 µm affects the differential phase-shift, which is the electromagnetic parameter most sensitive to dimensional errors. To this end, an ad-hoc assembling/testing procedure was conceived, based on the use of very precise gauge blocks. As shown in Figure 5(b), each plate implementing the ridge structures is aligned with the covers through two nominal alignment holes (indicated as # 1 and 2 in Figure 5(b)). The input lines are then connected to this sub-assembly, and the entire polarizer is assembled using M3 screws.

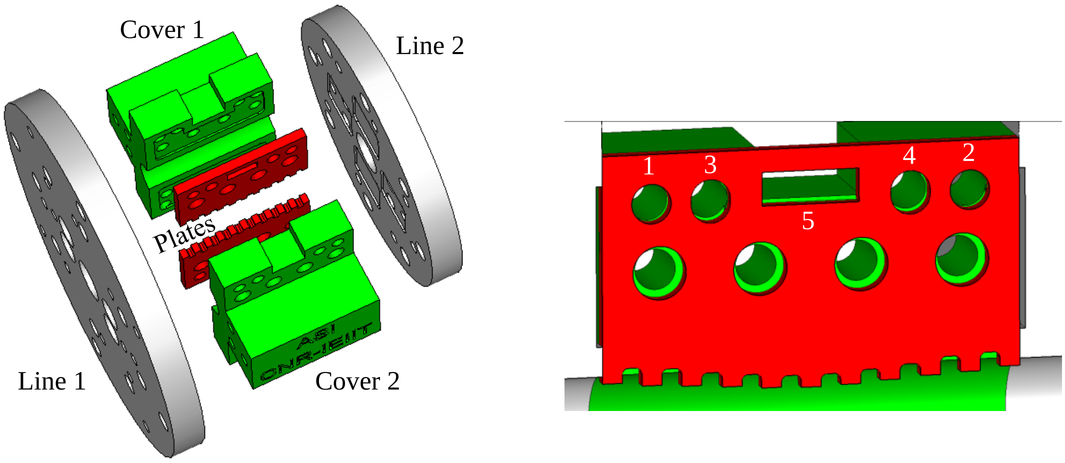

(a) (b)

Figure 5. Split-block mechanical layout of the polarizer. (a) 3D exploded view. (b) Detailed view of the alignment holes configuration used in the assembly. 1, 2: nominal alignment holes. 3, 4: elliptical holes for fine tuning. 5: housing slot for the gauge blocks.

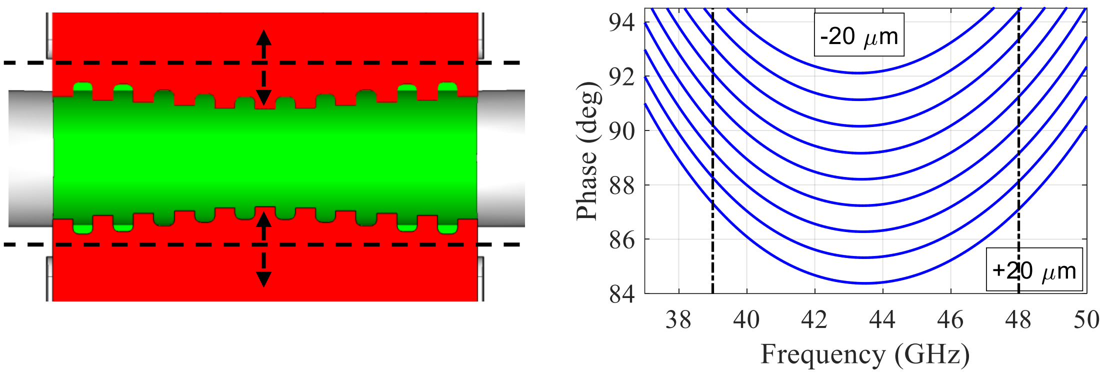

(a) (b)

Figure 6. Fine tuning of the differential phase-shift between the two principal directions. (a) Polarizer cut-view highlighting the plates displacement. Positive values correspond to outward displacements w.r.t. to the polarizer waveguide. (b) Simulated differential phase-shift values for displacements of the inner plates in steps of 5 μm.

If the measured differential phase-shift deviates from the design value by more than 0.5 deg, the polarizer assembly is slightly unscrewed, and two additional pins are inserted in the two elliptical holes #3 and #4 in Figure 5(b). Then, the nominal alignment pins are removed, and a gauge block is inserted in the housing slot. Since the elliptical holes are enlarged in the *y* direction, gauge blocks with different thickness can be inserted. As shown in Figure 6(a), this procedure allows us to vary the vertical position of the ridges w.r.t. to the covers (*i.e.*, the main circular waveguide) by ±20 μm in steps of 5 μm. The corresponding variations of the differential phase-shift are shown in Figure 6(b). The other electromagnetic parameters remain essentially unaffected.

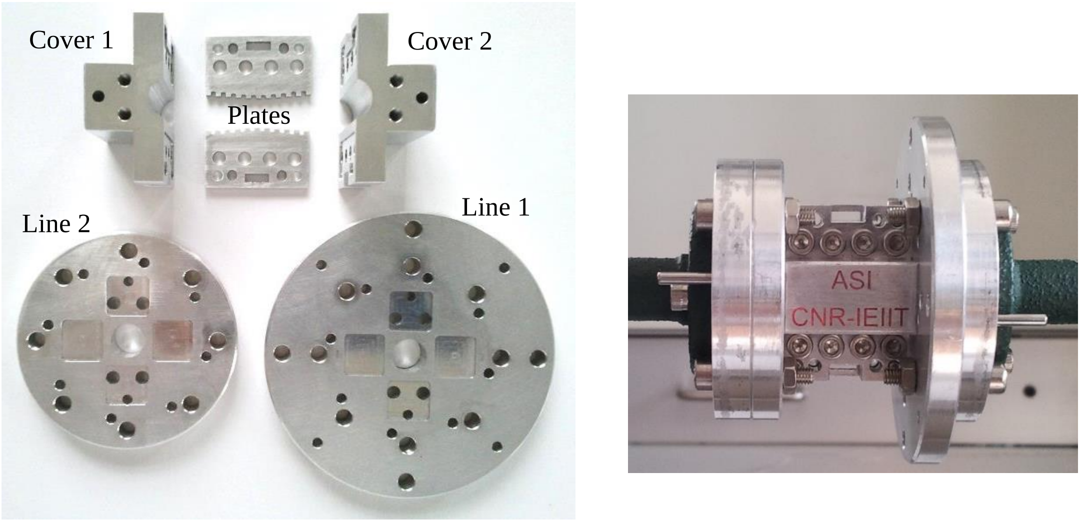

(a) (b)

Figure 7. Polarizer prototype. (a) Unassembled unit. (b) Assembled unit under test.

4. Measured Performance of the Polarizer Prototype

Before proceeding with the fabrication of the complete cluster of forty-nine polarizers (plus two spare units), a prototype was developed to verify the electromagnetic design and the manufacturing/assembling route. Furthermore, the prototype unit was used to investigate the need for silver-plating. The unassembled prototype (without silver-plating) is shown in Figure 7(a). All the parts were machined in 6061 aluminum alloy through milling or electrical-discharge machining. The outer diameters of Line 1 and Line 2 are not the same, since the interface flanges of the feed-horn and the OMT are different. The assembled prototype under test is shown in Figure 7(b), where the polarizer is attached to two circular-to-WR22 waveguide transitions. The latter were connected to the 2.4-mm cables of the Vector Network Analyzer (VNA) through WR22-to-2.4 adapters. The measurement setup was calibrated at the circular waveguide ports by the Thru-Reflection-Line (TRL) technique. Then, the polarizer was attached twice to the circular-to-WR22 waveguide transitions with its two principal directions aligned in turn along the direction of the TE_{11} polarization extracted by the transitions. During this procedure it was checked that no significant cable movement was occurring, in order to minimize uncertainty in the measurement of the phase/magnitude equalization between the two principal-polarization transmission coefficients.

According to the assembly procedure described in section 2.3, the polarizer was measured several times with the ridge plates shifted to different positions (inserting gauge blocks of different lengths), so as to achieve the best differential phase-shift $\bar{\phi}$ between the two principal polarizations. Figure 8(a) shows the measured curves of $\bar{\phi}$ for three different positions of the ridge plates in the case of the prototype without silver-plating. These curves correspond to the X-pol. transmission coefficients (in the operative basis) reported in Figure 8(b). For the optimized plate displacement of 5 μm, the scattering parameters (in the principal-polarization basis) as a function of frequency are shown in Figure 9. The predicted curves are also shown for

Table I. Comparison between predicted and measured scattering parameters of the polarizer prototype without and with silver-plating.

Parameter	Mean in-band value		
	Design	Measurement w/o silver-plating	Measurement with silver-plating
Reflection coefficient for L-pol. (dB)	-43.7	-42.8	-41.4
Reflection coefficient for C-pol. (dB)	-43.1	-43.0	-41.0
Insertion loss for L-pol. (dB)	-0.035	-0.033	-0.032
Insertion loss for C-pol. (dB)	-0.043	-0.047	-0.038
Insertion loss unbalance (dB)	0.008	0.014	0.006
Mean differential phase-shift (deg)	89.4	89.4	89.5
Relative phase-error (%)	3.5	3.4	3.7
X-pol. transmission in principal-pol. basis (dB)	-	-50.1	-45.3
X-pol. transmission in operative basis (dB)	-41.1	-41.4	-41.5

Simulations refer to an equivalent surface electrical resistivity ρ = 10 μΩ cm.

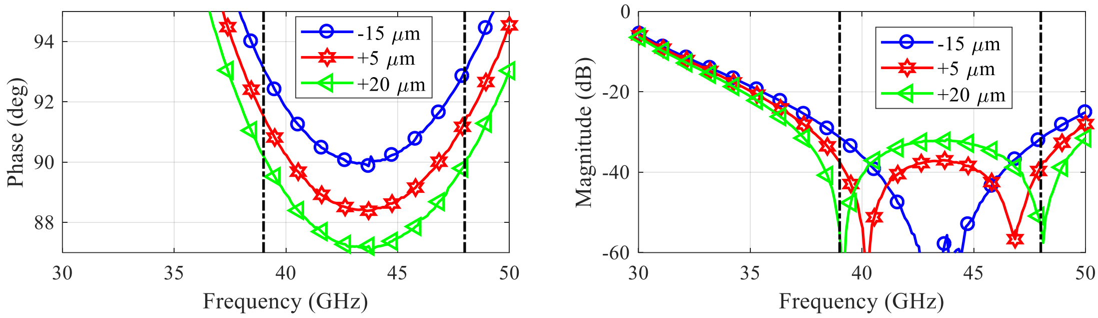

(a) (b)

Figure 8. Measured performance of the polarizer prototype (without silver plating) for different displacements of the ridges' plates. (a) Differential phase-shift between the transmission coefficients in the principal-polarization basis. (b) X-pol. transmission coefficients in the polarizer operative basis.

comparison. The simulations used an equivalent surface electrical resistivity ρ = 10 μΩ cm. In order to better interpret the measured results, the Root-Sum-Square (RSS) uncertainties of the measured parameters were evaluated. The RSS uncertainties were computed through the VNA uncertainty calculator [29], which implements the legacy methodology described in [30]. The corresponding confidence intervals are shown in Figure 9 as grey areas. To explore the possibility of further improving the polarizer electromagnetic performance, the prototype unit was silver-plated. The prototype surfaces were subjected to a soft pickling process and coated with a silver layer of 2-3 μm thickness. Table I reports the comparison between the predicted and measured in-band mean values of the scattering parameters for the prototype with and without silver-plating. The reduction in the insertion loss achieved through the silver-plating process was measured to be less than 0.01 dB, which is significantly smaller than the RSS uncertainty. The values of the X-pol transmission between the two polarizer principal-polarizations are at a similar level to the spurious X-pol. of the measurement setup (approximately -50 dB) that is generated by misalignments at the circular-waveguide ports of the setup and of the resistive vane inside the circular-to-WR22 transitions.

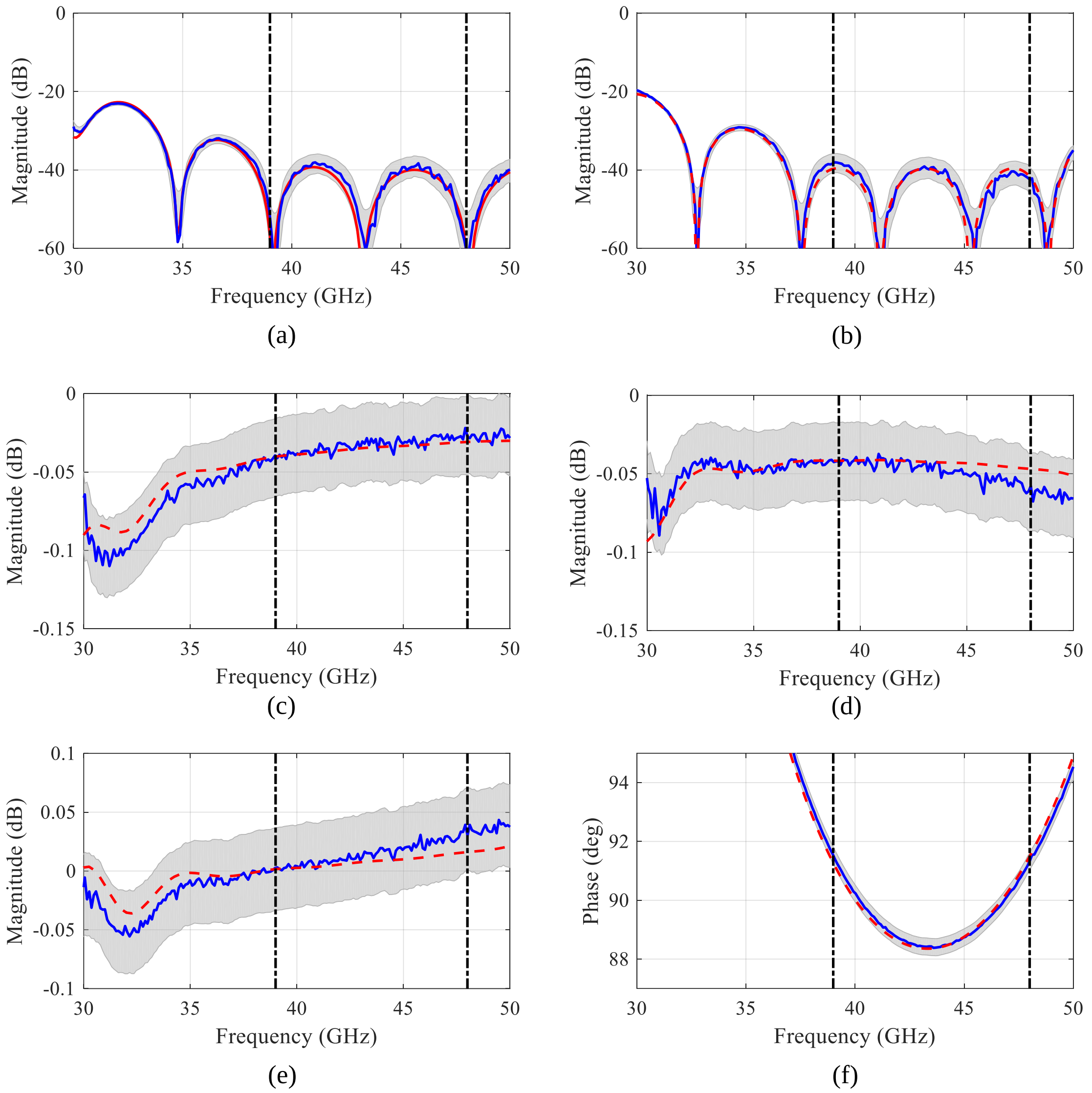

Figure 9. Comparison between the measured (blue solid lines) and predicted (red dashed lines) scattering coefficients in the principal-polarization basis of the polarizer prototype without silver plating. The simulations refer to an equivalent surface electrical resistivity $\rho = 10$ μΩ cm. The light-grey areas indicate the measurement RSS confidence intervals. (a) Reflection coefficient for the inductive polarization. (b) Reflection coefficient for the capacitive polarization. (c) Transmission coefficients for the inductive polarization. (d) Transmission coefficients for the capacitive polarization. (e) Amplitude unbalance between the transmission coefficients. (f) Differential phase-shift between the transmission coefficients.

On the basis of the measured scattering parameters, the elements of the Mueller submatrices ***H*** and ***K*** were evaluated according to (2.2)-(2.9). The corresponding in-band mean values are reported in Table II. As expected, because of the non-null measured values of the coefficients T_{LC} and T_{CL} (mainly due to the measurement errors in the order of -50 dB), the measured values of the elements H_{UQ}, K_{QV} range from -23.4 dB to -20.6 dB, while the measured coefficient K_{UI} is lower than -32.5 dB. In this respect, it has to be recalled that the Mueller submatrices ***H*** and ***K*** relate Stokes parameters that are quadratic entities. Consequently, coefficients T_{LC} and T_{CL} in the order of -50 dB lead in (2.7) and (2.9) to values of H_{UQ}, K_{QV} in the order of -

Table II. Comparison between predicted and measured coefficients of the Mueller sub-matrices ***H*** and ***K*** of the polarizer prototype without and with silver-plating.

Parameter	Mean in-band value		
	Design	Measurement w/o silver-plating	Measurement with silver-plating
H_{QQ} (dB)	-0.039	-0.040	-0.035
H_{UU} (dB)	-0.040	-0.041	-0.036
H_{UQ} (H_{QU}) (dB)	-	-23.4	-20.6
K_{QI} (dB)	-30.4	-27.7	-31.6
K_{UI} (dB)	-	-32.5	-35.4
K_{QV} (dB)	-	-23.5	-20.6
K_{UV} (dB)	-17.6	-17.8	-18.0

Simulations refer to an equivalent surface electrical resistivity ρ = 10 μΩ cm.

25 dB. In comparison, the measured values of the element K_{UI} are as low as -35.4 dB because this quantity is also minimized by the low losses and reflection coefficients of the polarizer, as discussed in sub-section 2.1 (see Equation (2.8)).

Since the insertion-loss improvement of the prototype provided by silver-plating was measured to be smaller than the measurement uncertainty, no silver-coating of the array units was carried out in order to minimize the risk of performance degradation induced by additional production processes. Additionally, the insertion loss difference between plated and unplated units is expected to be even lower at the operative temperature of 20 K, since electrical conductivity of metals increases at lower temperatures. Hence, with reference to Table II, the K_{QI} measured value of approximately -27.7 dB can be considered the worst-case polarizer contribution to the overall receiver chain operating at 20 K.

Figure 10. Cluster of the forty-nine manufactured polarizers ([3]).

Table III. Comparison between predicted and measured scattering coefficients of the polarizer cluster. Statistics of the in-band mean value over fifty-one units (*i.e.*, whole cluster augmented by two spare units).

Parameter	Mean in-band value		
	Design value	Mean value of the units	Standard deviation among the units
Reflection coefficient for L-pol. (dB)	-43.7	-42.5	0.4
Reflection coefficient for C-pol. (dB)	-43.1	-42.1	0.5
Insertion loss for L-pol. (dB)	-0.035	-0.034	0.007
Insertion loss for C-pol. (dB)	-0.043	-0.045	0.007
Insertion loss unbalance (dB)	0.008	0.011	0.003
Mean differential phase-shift (deg)	89.4	89.3	0.3
Relative phase-error (%)	3.5	3.4	0.1
X-pol. transmission in principal-pol. basis (dB)	-	-48.7	1.4
X-pol. transmission in the operative basis (dB)	-41.1	-41.1	1.2

Simulations refer to an equivalent surface electrical resistivity ρ = 10 μΩ cm.

5. Measured Performance of the Polarizer Cluster

On the basis of the positive assessment of the polarizer design and manufacturing route achieved through the prototyping activities reported in section 4, the whole cluster of forty-nine elements shown in Figure 10 was manufactured. Redundancy was provided by manufacturing two additional spare units. Each unit was assembled and tested according to the procedure applied to the prototype.

Table III compares the predicted and measured in-band mean values of the scattering coefficients of the fifty-one manufactured polarizers. Specifically, Table III reports the statistics of the measured performance in terms of mean value and standard deviation among the units. The complete sets of measured scattering coefficients in the principal-polarization and operative bases (see Figure 1) versus frequency are shown in Figure 11 and Figure 12, respectively. Because of the care taken in the selected electromagnetic design and manufacturing route, the measured performances of the polarizer cluster are in good agreement with both the design values and the prototype measurements. Notably, the performance deviations across the units are almost within the RRS measurement uncertainty values. The statistics of the measured in-band values of the Mueller sub-matrices $\boldsymbol{H}$ and $\boldsymbol{K}$ are compared with the predicted performance in Table IV. This table confirms that the measured Stokes parameter transfer function of the whole cluster is in line with the prototype results. Specifically, the coefficients K_{QI} and K_{UI}, which are crucial to the instrument performance, have mean values of -28.8 dB and -31.2 dB with a standard deviation among the units that is smaller than 1 dB.

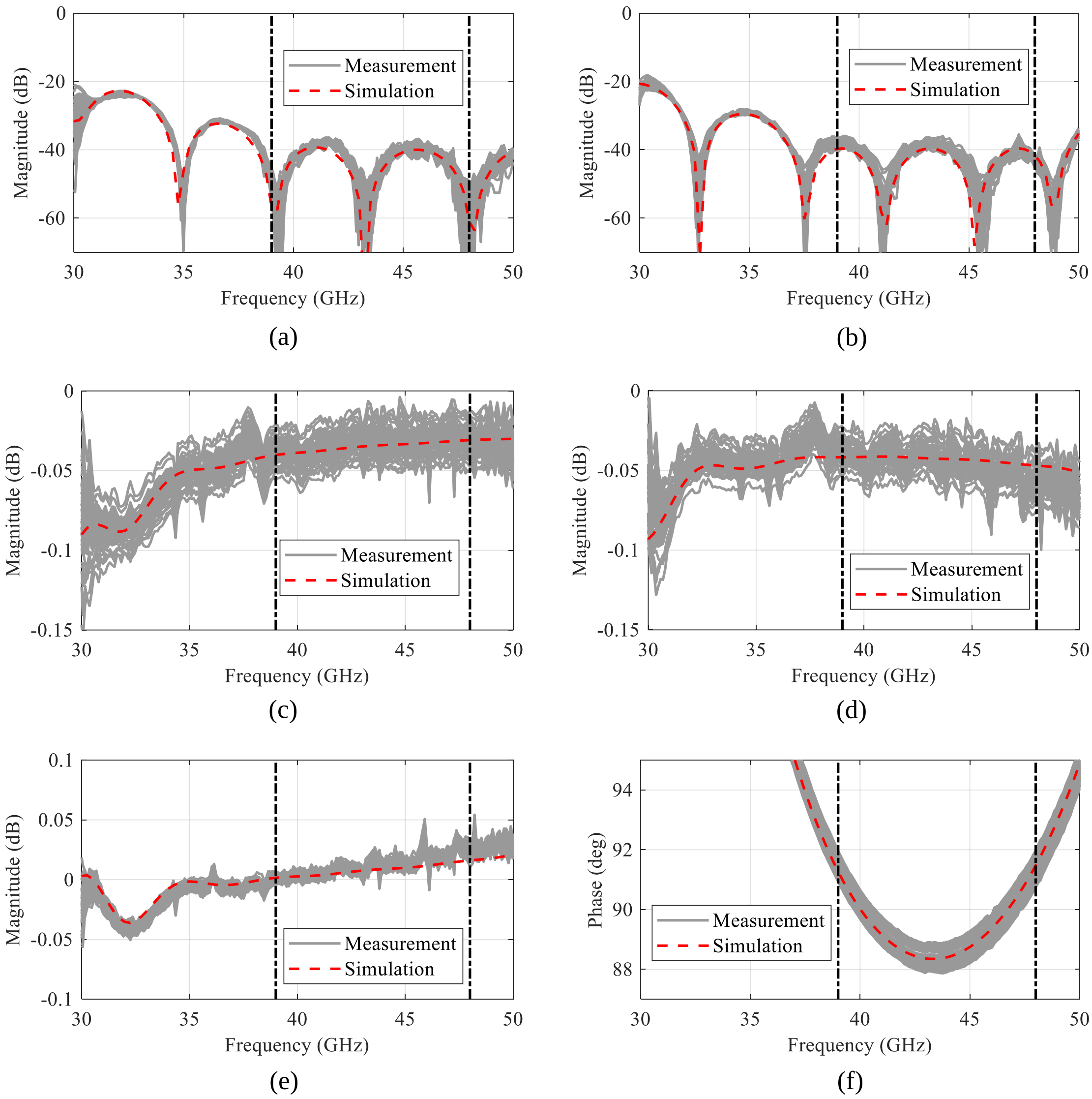

Figure 11. Measured scattering coefficients in the principal-polarization basis of the fifty-one polarizer units (*i.e.*, forty-nine for the focal plane array plus two spare units). (a) Reflection coefficients for the inductive polarization. (b) Reflection coefficients for the capacitive polarization. (c) Transmission coefficients for the inductive polarization. (d) Transmission coefficients for the capacitive polarization. (e) Amplitude unbalances between the transmission coefficients. (f) Differential phase-shift between the transmission coefficients.

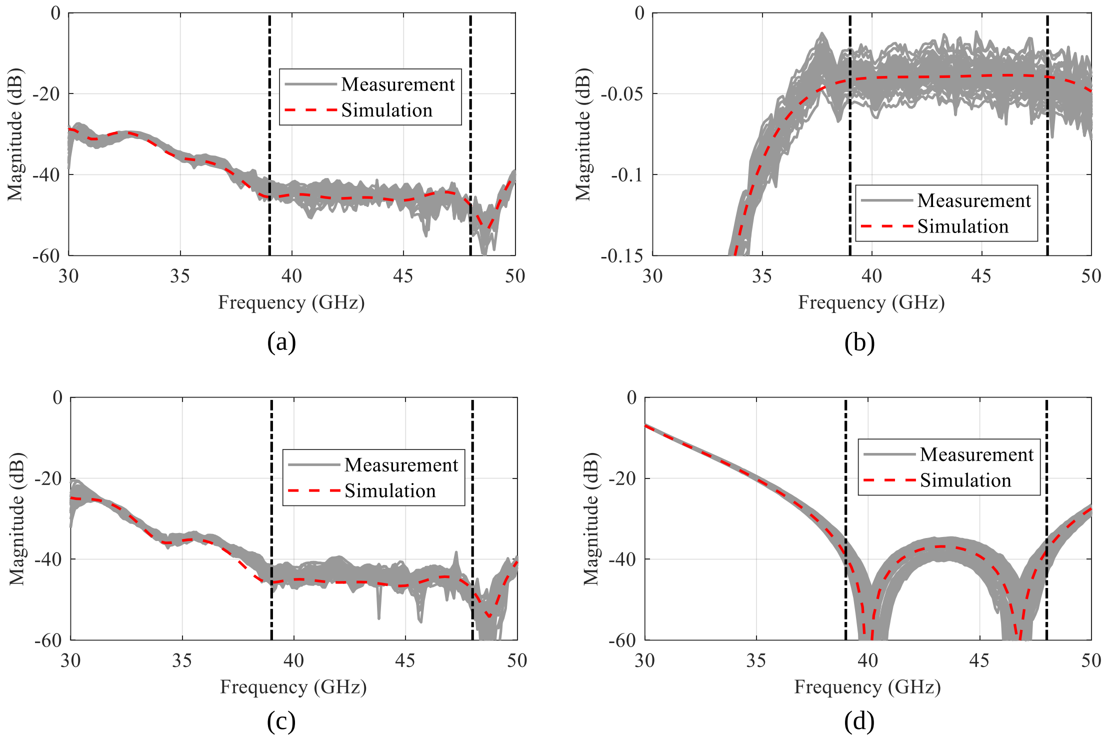

Figure 12. Measured scattering coefficients in the operative basis of the fifty-one polarizer units (*i.e.*, forty-nine for the focal plane array plus two spare units). (a) Co-polar reflection coefficients. (b) Co-polar transmission coefficients. (c) X-pol. reflection coefficients. (d) X-pol. transmission coefficients.

Table IV. Comparison between predicted and measured coefficients of the Mueller sub-matrices ***H*** and ***K*** of the polarizers cluster. Statistics of the in-band means value over the fifty-one polarizer units (*i.e.*, forty-nine for the focal plane array plus two spare units).

Parameter	Mean in-band value		
	Design value	Mean value of the units	Standard deviation among the units
H_{QQ} (dB)	-0.039	-0.040	0.007
H_{UU} (dB)	-0.040	-0.041	0.007
H_{UQ} (H_{QU}) (dB)	-	-23.52	0.46
K_{QI} (dB)	-30.4	-28.84	0.89
K_{UI} (dB)	-	-31.19	0.78
K_{QV} (dB)	-	-23.54	0.43
K_{UV} (dB)	-17.6	-17.59	0.58

Simulations refer to an equivalent surface electrical resistivity $\rho = 10\ \mu\Omega$ cm.

6. Conclusions

In this paper, the design, manufacture, assembly and testing of the Q-band polarizers of the LSPE-Strip instrument have been described. These activities were informed by analysis of the specific figures-of-merit relevant for polarizers used in a dual-circular-polarization correlation receiver. The development plan was successfully completed and proved to be effective at minimizing systematic errors and instrument uncertainties introduced by the polarizers in the receiver chains. Specifically, the leakage of total intensity I in to the measured linearly-polarized Stokes parameters Q and U is smaller than -28 dB (with a standard deviation less than 1 dB) for all the array units. While this spurious leakage is low, its effect on the overall LSPE-Strip receiver performance and the identification of possible mitigation strategies will be the subject of a forthcoming paper.

Acknowledgments

The LSPE–Strip instrument has been developed thanks to the support of ASI contract I/022/11/1 and Agreement 2018-21-HH.0 and by funding from INFN (Italy).

References

[1] Planck Collaboration, *Planck 2018 results. I. Overview, and the cosmological legacy of Planck*, Astronomy & Astrophysics, 2020, 641, A1. DOI: 10.1051/0004-6361/201833880

[2] M. Kamionkowski, and E. D. Kovetz, *The quest for B modes from inflationary gravitational waves*, Annu. Rev. Astron. Astrophys. **54** (2016) 227–69. DOI: 10.1146/annurev-astro-081915-023433

[3] The LSPE collaboration, G. Addamo, P. A. R. Ade, C. Baccigalupi, A. M. Baldini, P. M. Battaglia et al., *The large scale polarization explorer (LSPE) for CMB measurements: performance forecast*, JCAP **2021** (Aug. 2021). DOI: 10.1088/1475-7516/2021/08/008

[4] C. Franceschet, F. Del Torto, F. Villa, S. Realini, R. Bongiolatti et al., *The LSPE-Strip feed horn array*, JINST **17** (Jan. 2022) 1-28. DOI: 10.1088/1748-0221/17/01/P01029

[5] J. Uher, J. Bornemann, and U. Rosenberg, *Waveguide components for antenna feed systems: Theory and CAD*, Arthech House, Norwood, MA 1993

[6] G. Virone, O. A. Peverini, M. Lumia, G. Addamo and R. Tascone, *Platelet orthomode transducer for Q-band correlation polarimeter clusters*, IEEE Trans. Microw. Theory Techn. **62** (Jul. 2014) 1487-1494. DOI: 10.1109/TMTT.2014.2325793

[7] C. Bischoff, A. Brizius, I. Buder, Y. Chinone, K. Cleary, et al. et al., *The Q/U imaging experiment instrument*, Astrophys. J. **768** (Apr. 2013) 1-28. DOI: 10.1088/0004-637X/768/1/9

[8] Mennella et al. 2022, *The LSPE-Strip focal plane instrument*, in preparation for JINST Special Issue 'The LSPE/Strip instrument description and testing'

[9] M. Z. Farooqui, A*nalysis and design of microwave and millimeter-wave passive devices for scientific instrumentation*, PHD Dissertation, 2014. DOI: 10.6092/POLITO/PORTO/2541493

[10] G. Bertin, B. Piovano, L. Accatino and M. Mongiardo, *Full-wave design and optimization of circular waveguide polarizers with elliptical irise*s, IEEE Trans. Microw. Theory Techn. **50** (Apr. 2002) 1077-1083. DOI: 10.1109/22.993409

[11] Y. Liu, F. Li, X. Li and H. He, *Design and optimization of wide and dual band waveguide polarizer*, in *2008 Global Symp. on Millimeter Waves*, Apr. 21-24, 2008, Nanjing, China. DOI: 10.1109/GSMM.2008.4534654

[12] K. K. Chan and H. Ekstrom, *Dual band/wide band waveguide polarizer*, in 2000 Asia-Pacific Microw. Conf. (Cat. No.00TH8522), Dec. 3-6, 2000, Sydney, Australia. DOI: 10.1109/APMC.2000.925721

[13] O. A. Peverini, G. Virone, G. Addamo, R. Tascone, *Development of passive microwave antenna-feed systems for wide-band dual-polarisation receivers*, IET Microw. Antennas Propag. **5** (Jun. 2011) 1008 – 1015. DOI: 10.1049/iet-map.2010.0340

[14] N. Yoneda, R. Miyazaki, I. Matsumura and M. Yamato, *A design of novel grooved circular waveguide polarizers*, IEEE Trans. Microw. Theory Techn. **48** (Dec. 2000) 2446-2452. DOI: 10.1109/22.898996

[15] N. Luo, X. Yu, G. Mishra and S. K. Sharma, *A millimeter-wave (V-band) dual-circular-polarized horn antenna based on an inbuilt monogroove polarizer*, IEEE Antennas Wireless Propag. Lett. **19** (Nov. 2020) 1933-1937. DOI: 10.1109/LAWP.2020.3015745

[16] I. Agnihotri and S. K. Sharma, *Design of a compact 3-D metal printed Ka-band waveguide polarizer*, IEEE Antennas Wireless Propag. Lett. **18** (Dec. 2019) 2726-2730. DOI: 10.1109/LAWP.2019.2950312

[17] S. Y. Eom and Y. B. Korchemkin, *A new comb circular polarizer suitable for millimeter-band application*, ETRI Journal **28** (Oct. 2006). DOI: https://doi.org/10.4218/etrij.06.0206.0110

[18] G. Virone, R. Tascone, O. A. Peverini and R. Orta, *Optimum-iris-set concept for waveguide polarizers*, IEEE Microw. Wireless Compon. Lett. **17** (Mar. 2007) 202-204. DOI: 10.1109/LMWC.2006.890474

[19] Shih-Wei Wang, Chih-Hung Chien, Chun-Long Wang and Ruey-Beei Wu, *A circular polarizer designed with a dielectric septum loading*, IEEE Trans. Microw. Theory Techn. **52** (Jul. 2004) 1719-1723. DOI: 10.1109/TMTT.2004.830487

[20] M. Zheng and J. Qi, *A low-cost high-performance dual-band diaphragm circular polarizer*, in 2020 IEEE Intern. Symp. Antennas Propag. and North American Radio Science Meeting, Jul. 5-10, 2020, Montreal, Canada. DOI: 10.1109/IEEECONF35879.2020.9329806

[21] A. Tribak, A. Mediavilla, J. L. Cano, M. Boussouis and K. Cepero, *Ultra-broadband low axial ratio corrugated quad-ridge polarizer*, in 2009 Eur. Microw. Conf. (EuMC), Sept. 29 - Oct. 1, 2009, Rome, Italy. DOI: 10.23919/EUMC.2009.5295927

[22] G. Virone, R. Tascone, O. A. Peverini, G. Addamo and R. Orta, *Combined-phase-shift waveguide polarizer*, IEEE Microw. Wireless Compon. Lett., **18** (Aug. 2008) 509-511. DOI: 10.1109/LMWC.2008.2001005

[23] C. L. H. Hull, R. Plambeck and G. Engargiola, *1 mm Dual-polarization science with CARMA*, in 2011 XXXth URSI General Assembly and Scientific Symp., Aug. 13-20, 2011, Istanbul, Turkey. DOI: 10.1109/URSIGASS.2011.6051255

[24] G. Pisano, R. Nesti, M. W. Ng, A. Orfei, D. Panella and P. Wilkinson, *A novel broadband Q-band polarizer with very flat phase response*, Journal Electrom. Waves Applications **26** (Jul. 2012) 707-715. DOI: 10.1080/09205071.2012.710795

[25] O. Deparis and P. Lambin, *Alternative expression of the Bloch wave group velocity in loss-less periodic media using the electromagnetic filed energy*, Journal of Modern Optics **65** (2018) 213-220. DOI: 10.1080/09500340.2017.1384513

[26] O. A. Peverini, G. Addamo, G. Virone, R. Tascone, R. Orta, *A spectral-element method for the analysis of 2-D waveguide devices with sharp edges and irregular shapes*, IEEE Trans. Microw. Theory Techn. **59** (Jul. 2011) 1685 – 1695. DOI: 10.1109/TMTT.2011.2144991

[27] G. Virone, R. Tascone, M. Baralis, O. A. Peverini, A. Olivieri and R. Orta, *A novel design tool for waveguide polarizers*, IEEE Trans. Microw. Theory Techn. **53** (Mar. 2005) 888-894, DOI: 10.1109/TMTT.2004.842491

[28] P. Bradley P. and R. Radebaugh, *Properties of selected materials at cryogenic temperatures*, CRC Press, Boca Raton, FL 2013. https://tsapps.nist.gov/publication/get_pdf.cfm?pub_id=913059

[29] Keysight Technologies, *VNA uncertainty calculator*, https://www.keysight.com

[30] D. Blackham, *Trends for computing VNA uncertainties*, in 89th ARFTG Microw. Meas. Conf., Jun. 9, 2017, Honolulu, USA, DOI: 10.1109/ARFTG.2017.8000833